CrossMark

Evolution of multilayered scale structures during high temperature oxidation of $ZrSi_2$

Hwasung Yeom and Ben Maier
Department of Engineering Physics, University of Wisconsin-Madison, Madison, Wisconsin 53706, USA
Robert Mariani and David Bai
Idaho National Laboratory, Idaho Falls, Idaho 83402, USA
Kumar Sridharan[a)]
Department of Engineering Physics, University of Wisconsin-Madison, Madison, Wisconsin 53706, USA

(Received 13 June 2016; accepted 15 September 2016)

The oxidation behavior of bulk $ZrSi_2$ at 700, 1000, and 1200 °C in ambient air has been investigated. Parabolic to cubic oxide layer growth kinetics was confirmed by weight gain measurements and the average oxide layer thickness was 470 nm, 6.7 μm, and 37 μm at 700 °C, 1000 °C, and 1200 °C, respectively, after 5 h oxidation tests. Evolution of compositionally modulated nano/micro structures was confirmed in the oxide layer. At 700 °C, Si diffusion resulted in discontinuous Si-rich oxide phases in amorphous Zr–Si–O matrix. At 1000 °C, complex multilayered structures such as fine and coarse irregular spinodal structures, wavy Si-rich oxide, and Si-rich islands evolved. At 1200 °C, additional nucleation of nanoscale ZrO_2 particulate phase was observed. The spinodal structures were confirmed to be crystalline ZrO_2 and amorphous SiO_2, and the thermodynamic driving force for phase evolution has been explained by extension of liquid miscibility gap in the binary ZrO_2–SiO_2 phase diagram.

I. INTRODUCTION

In light water reactors (LWR), zirconium-alloy (Zr-alloy) fuel claddings have been widely used for over four decades due to the excellent neutron transparency of Zr, and combination of corrosion resistance and mechanical properties in normal operating conditions.[1] However, in high temperature environments (1000 °C or higher) as may be the case during accident scenarios, significant degradation of the Zr-alloy cladding occurs. Profuse exothermic oxidation occurs (with associated hydrogen production) leading to a loss in mechanical integrity of the cladding. Furthermore, zirconium-oxide undergoes phase transformations as the temperature rises, which promotes its spallation and exacerbates cladding degradation.[2–5] Efforts to address this challenge have been aimed at replacing Zr-alloy as cladding material with other materials such as FeCrAl alloys and SiC–SiC composites.[2,6–9] Another approach involves deposition of oxidation-resistant coatings on Zr-alloy cladding. In this regard, chromium,[10,11] Ti_2AlC,[12] and TiN[13] coatings have been investigated.

It is well known that transition metal-silicides have outstanding oxidation resistance and structural properties at high temperatures. For example, $MoSi_2$ has been extensively studied on account of its outstanding oxidation resistance.[14] However, this material has been reported to suffer from accelerated pest oxidation at low temperatures resulting in a porous and nonprotective oxide scale.[15,16] $ZrSi_2$ has been studied to a much lesser extent, but appears to be a more appropriate candidate for a coating for the nuclear fuel cladding application from the standpoints of neutronics and greater compatibility with the underlying Zr-alloy substrate due to its oxophilic nature which is expected to result in better bonding to the native oxide film on the Zr-alloy. Moreover, $ZrSi_2$ has high Young's modulus (~200 GPa) and high compressive yield strength at high temperatures (~200 MPa at 1000 °C).[17] However, there have been only limited studies on the evaluation of oxidation behavior of $ZrSi_2$ at high temperatures. It has been reported that oxidation of $ZrSi_2$ in dry oxygen and steam does not result in a continuous SiO_2 layer, differing in this regard from other silicides ($CoSi_2$, $CrSi_2$, $NiSi_2$, $PtSi_2$, and $TiSi_2$) regardless of oxidation temperature.[18] The long term isothermal oxidation (600–1100 °C for 160 h) of aluminum alloyed (4 at.% addition) $ZrSi_2$ showed high oxidation resistance with two oxidation stages above 700 °C: early stage (formation of $ZrSiO_4$, ZrO_2) and steady-state stage (formation of Al_2O_3).[19,20] Thermogravimetry and differential thermal analysis experiments of $ZrSi_2$ powders up to 1450 °C suggest complex step reactions with combination of ZrO_2, SiO_2, and $ZrSiO_4$ formation.[21] Nevertheless, the oxidation data of bulk $ZrSi_2$ at high temperature are still limited.

Contributing Editor: Yanchun Zhou
[a)]Address all correspondence to this author.
e-mail: kumar@engr.wisc.edu
DOI: 10.1557/jmr.2016.363

 © Materials Research Society 2016

https://doi.org/10.1557/jmr.2016.363 Published online by Cambridge University Press

In this study, the oxidation behavior of dense bulk forms of $ZrSi_2$ in high temperature air (700, 1000, and 1200 °C) has been explored. A temperature of 700 °C was chosen to determine whether material degradation at low temperature occurs like $MoSi_2$ while higher temperatures (1000 and 1200 °C) simulate a postulated loss of coolant accident scenario in LWR.[22] In addition, Zircaloy-4 (Zry-4) was also oxidized under similar conditions as a base-line for comparison with $ZrSi_2$. All oxidized samples were rigorously characterized with the goal of understanding compositional and morphological evolution of microoxide and nanooxide structures.

II. EXPERIMENTAL

A. Materials

Commercially available dense $ZrSi_2$ (American Elements Inc., Los Angeles, CA) with a reported purity of >99.5% and Zircaloy-4 plate (ATI Wah Chang, Albany, OR, referred to as Zr-4 henceforth) were procured for this study. The density of the dense $ZrSi_2$ was about 95% of theoretical densities,[23] respectively. The phases in the as-received materials were confirmed by x-ray diffraction analysis (XRD), but few micron-sized Si particles were revealed in as-received $ZrSi_2$ matrix as an impurity. All $ZrSi_2$ samples were cut and ground into approximately 12.7 × 12.7 mm^2, 6.4 mm thick square coupons, and Zr-4 coupons were 3.2 mm thick.

B. Air oxidation tests

All six faces on the samples were ground progressively with 320, 600, 800, and 1200 grit SiC papers and then ultrasonically cleaned with methanol and acetone. The dense $ZrSi_2$ and the Zry-4 samples were exposed at 700, 1000, and 1200 °C in stagnant ambient air. The samples were removed each hour for weight change measurements (as an initial measure of the extent of oxidation) performed with Satorius microprecision balance (model#CPA26P) with 0.002 mg resolution. The fast cooling with ambient air was conducted because slow cooling may not be able to preserve microstructures that evolved at high temperatures and to minimize this possibility of any changes during cooling.

C. Characterization

Surface morphology and evolution of oxide structures in cross-section were characterized by Zeiss LEO Scanning Electron Microscope (SEM; Carl Zeiss AG, Oberkochen, Germany) integrated with Energy Dispersive Analysis System (EDS). XRD (Bruker Corporation, Billerica, Massachusetts) with Cu K_α radiation was performed to identify oxide product phases and the very near-surface composition was evaluated by Thermo-Scientific Kα x-ray Photoemission Spectroscopy (XPS; Thermo Fisher Scientific, Waltham, Massachusetts). To identify oxidized structures at high magnification and resolutions, thin foils of the sample surface were lifted out by a Zeiss Auriga Focus Ion Beam (FIB; Carl Zeiss AG) milling and imaged with a Tecnai 12 Transmission Electron Microscope (TEM; FEI Company, Hillsboro, Oregon) and Titan Scanning TEM in conjunction with EDS (STEM-EDS; FEI Company).

III. EXPERIMENTAL RESULTS

A. Oxidation kinetics and oxidation products

The kinetics of oxidation of the dense $ZrSi_2$ was determined by weight change measurements at each hour during oxidation. The weight gain values (per unit area of the sample) of Zry-4 and dense $ZrSi_2$ are shown in Fig. 1. As may be noted, the weight gain of the dense $ZrSi_2$ is negligible compared to that of the Zry-4 at the high temperatures. The Zry-4 showed the formation of a thick oxide scale and its spallation led to weight reduction at 1000 °C (4 h) and 1200 °C (3 h) as shown in Fig. 1(a). On the other hand, the dense $ZrSi_2$ appeared to be stable without significant degradation at the high temperatures.

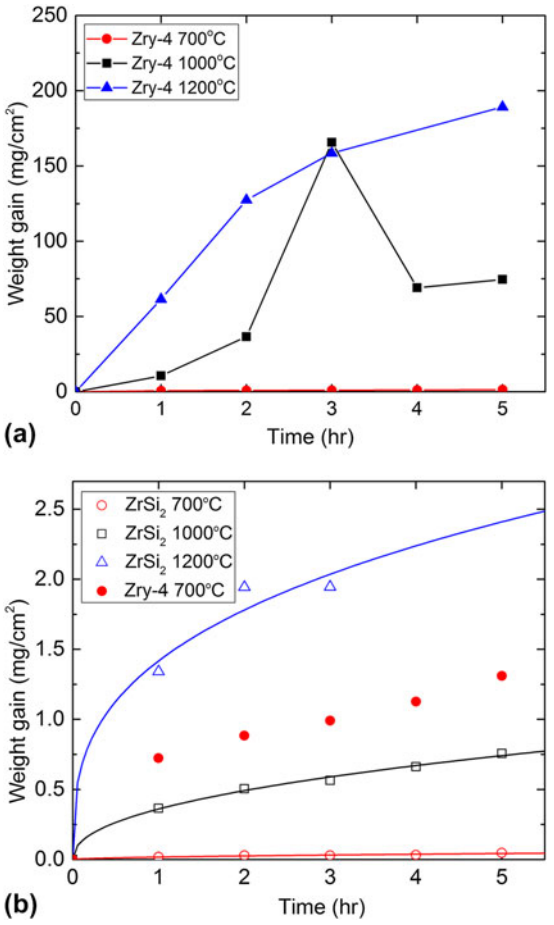


FIG. 1. Weight gain versus time for (a) Zry-4 and (b) dense $ZrSi_2$ samples constructed with least square fits at 700, 1000, and 1200 °C in air.

https://doi.org/10.1557/jmr.2016.363 Published online by Cambridge University Press

It is worth noting that no pest oxidation was observed on the surface of the $ZrSi_2$ samples. Minor chipping on the edge of the dense $ZrSi_2$ samples was observed at 1200 °C after 3 h oxidation. Therefore, the weight gain values at 5 h have not been reported in Fig. 2(b). The general oxidation kinetics follows a power law. The oxidation kinetics at 700 and 1000 °C follow approximately a parabolic rate law while at 1200 °C follows more closely the cubic growth rate law. More protective nature with increasing temperatures has been reported in $MoSi_2$ and $TiSi_2$ as well, resulting from denser SiO_2 formation.[15,24,25] The weight gain relationships are empirical and were plotted with the limited data points so that it is difficult to elucidate physical and chemical processes of the oxide growth. Nevertheless, the weight gain trends imply that the $ZrSi_2$ oxidation process is controlled by the diffusion of charged species (e.g., Si^{4+}, O^{2-}) through the oxide dictating the oxide growth rate.[26]

The oxide layer thickness was measured in SEM cross-sectional images and shown in Fig. 2. The average oxide layer thickness of the dense $ZrSi_2$ at 700 °C, 1000 °C, and 1200 °C for 5 h oxidation was determined to 470 nm, 6.7 μm, and 37 μm, respectively. In addition, the oxide layer thickness at 1000 °C for 15 h oxidation was 12 μm, which considered together with other exposure times at this temperature is indicative of parabolic oxidation kinetics at 1000 °C. Furthermore, no spallation and delamination of the oxide layer were observed and only minor cracks were identified in unreacted $ZrSi_2$ matrix underneath the oxide scale at 1200 °C possibly due to thermal cycling due to periodic removal of samples from the furnace.

Although thickness of the $ZrSi_2$ oxide layer formed at high temperatures is significantly lower than that formed on Zr-4, the oxide scale is much thicker than for $TaSi_2$, $MoSi_2$, and WSi_2 in the similar oxidation tests (1000 °C air) reported in literature.[27,28] One of possible reason for this is the thermodynamically favored ZrO_2 formation in $ZrSi_2$ oxidation. Fig. 3 shows Gibbs free energy formation of oxide per a mole of O_2 of Si as well as Ta, Ti, Mo, W, and Zr, which was calculated by HSC Chemistry thermodynamics software. In these other metal-silicides except for Ti, selective oxidation of Si leads to the formation of a continuous oxidation resistant SiO_2 layer[29] while the absence of continuous SiO_2 layer in $ZrSi_2$ may result in relatively faster oxide growth. Likewise, $TiSi_2$ has at least five times higher oxidation rate compared to $MoSi_2$.[20]

The phases present in the oxide layer formed at different temperatures for 5 h exposure were identified by full-theta XRD analysis and the results are shown in Fig. 4. At 700 °C oxidation [Fig. 4(a)], pronounced diffracted peaks stemming from unreacted $ZrSi_2$ and weak Si and monoclinic ZrO_2 (m-ZrO_2) peaks were identified. At 1000 °C [Figs. 4(b)] and 1200 °C [Fig. 4(c)] oxidation, intensity of m-ZrO_2 was remarkably increased and weak Si peaks were also seen. Grazing incidence XRD scan (2° incident beam angle) showed the same results. For higher temperatures, the intensity of the strongest m-ZrO_2 peak at 28° (−111) gets sharper but the $ZrSi_2$ strongest peak at 39° (131) gets weaker and broader, which corresponds to thicker ZrO_2 oxide layer at higher temperature. In addition, absence of peaks of thermodynamically favored SiO_2 and zircon ($ZrSiO_4$) phases observed in Zr–Si–O system does not preclude their presence, since they may be present as amorphous phases. During the selective oxidation of Zr in $ZrSi_2$, some Si may be newly formed as an intermediate product which represents the weak silicon peak at 47° (220). Geßwein et al.[21] postulated selective oxidation producing SiO_2 and Si at low temperature [as shown in Eq. (1)] from thermogravimetric experiments of $ZrSi_2$ powders oxidation in air.

$$ZrSi_2 + O_2 \rightarrow ZrO_2 + (2-y)SiO_x + ySi \quad (500\ ^{\circ}C < T < 800\ ^{\circ}C) \quad (1)$$

Additionally, it is not surprising that tetragonal-zirconia phase which is stable above 1000 °C based on Zr–O binary phase diagram[30] is not observed in Fig. 4. This is because our XRD analysis was conducted at room temperature so that most tetragonal zirconia transformed to monoclinic zirconia during cooling.[22]

B. Microstructural evolution oxide layer in the oxidized $ZrSi_2$

Given that both Zr and Si have very negative Gibbs free energy of oxide formation of each oxide and possible selective and nonselective oxidations of Zr in $ZrSi_2$ creates the potential to produce complex multilayered

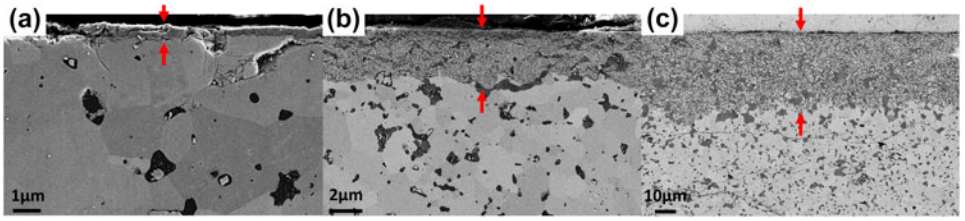


FIG. 2. Cross-sectional SEM images of the dense $ZrSi_2$ at (a) 700 °C, (b) 1000 °C, and (c) 1200 °C for 5 h exposure in air. The red arrows indicate the oxide layer between a mounting resin and unreacted $ZrSi_2$.

https://doi.org/10.1557/jmr.2016.363 Published online by Cambridge University Press

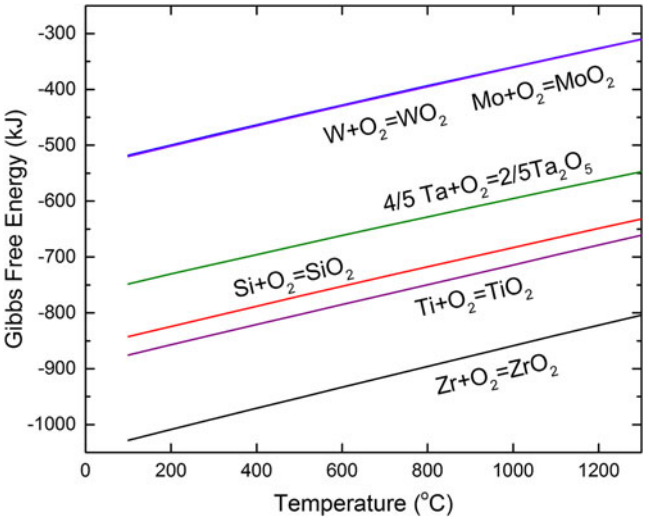


FIG. 3. Gibbs free energies of oxide formation for Zr, Ti, Si, Ta, W, and Mo per 1 mole O_2, calculated by HSC Chemistry thermodynamics software.

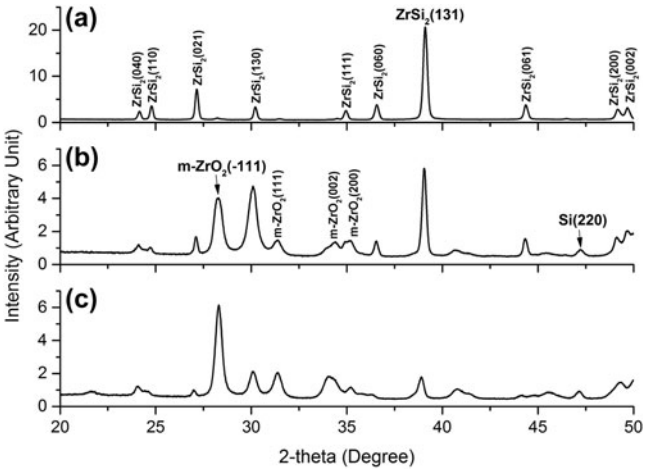


FIG. 4. XRD patterns of the $ZrSi_2$ oxidized at (a) 700 °C, (b) 1000 °C, and (c) 1200 °C for 5 h showing monoclinic zirconia, silicon, and unreacted $ZrSi_2$ peaks.

structure, which may be beneficial for protection of Zr-alloy fuel cladding under accident conditions.

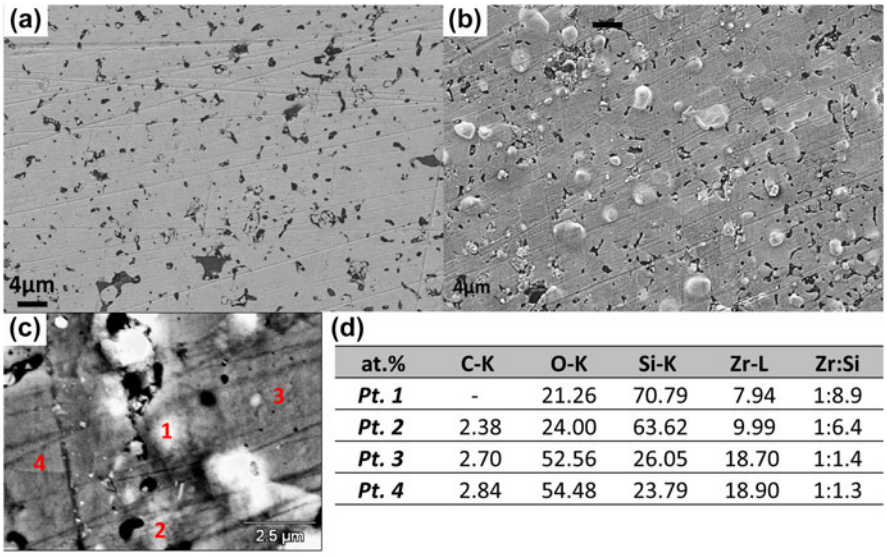
1. Surface morphology evolution

To investigate the compositional and morphological evolution of the oxide layer at high temperatures, plan-view SEM-EDS examinations were first performed for samples exposed to each of the temperatures for 5 h. Figure 5(a) shows SEM image of the surface of the as-received $ZrSi_2$ and Fig. 5(b) shows surface of $ZrSi_2$ sample that was subject to oxidation at 700 °C for 5 h. Figures 5(c) and 5(d) show results of EDS analysis of the oxide layer. Micron-sized spherical phases were observed to evolve on the oxidized surface [Fig. 5(b)]. Semiquantitative EDS point scan confirmed that there were local variations in the concentration of Si, Zr, and O on the surface and the spherical phases were enriched in Si [i.e., point 1 and 2 in Fig. 5(c)]. This represents a significantly higher Si concentration than in the as-received $ZrSi_2$ for which the Zr-to-Si ratio was 1:2.4 as determined by our XPS, to be discussed later. Therefore, the micron-scale spherical phases appear to be Si-rich oxides formed by Si diffusion from the surrounding area.

On surfaces oxidized at higher temperatures, the surface morphology was different as shown in Fig. 6 for samples oxidized at 1000 and 1200 °C. The Si-rich humps were not clearly identified but nanoscale precipitation of oxide phase particulates (40–100 nm in size) appeared, particularly, on the surface of samples oxidized at 1200 °C [Fig. 6(b)]. The imaging contrast between the background matrix and oxide particulates suggests differences in their compositions and TEM-EDS analysis determined that these nanosized particulates were ZrO_2 as will be discussed later. At 1000 °C, the fine oxide particles also emerged on the surface but the size of structure was too small to be quantified in the SEM image.

To understand the structural evolution at the surface during high temperature, XPS analysis was performed. The chemical states of Si, Zr, and O were acquired over a 400 μm diameter circular region on the surface of samples oxidized at each of the temperatures for 5 h and the results are shown in Fig. 7. The intensity of Si 2*p* binding energy peak increases with increasing oxidation temperature—the peak binding energy shifted +1 eV (102.8 eV → 103.8 eV) between samples oxidized at 700 °C and those oxidized at higher temperatures (1000 and 1200 °C). On the other hand, signal intensity of the Zr $3d_{3/2}$ and Zr $3d_{5/2}$ binding energies decreased with increasing oxidation temperature. Here, the peak values shifted −0.7 eV at 1000 °C compared to 700 °C (183.6 eV → 182.9 eV). The O 1*s* binding energy associated with the elements showed the same trends with respect to temperature. The intensity of O 1*s* binding energy associated with Zr atom decreased but that of Si atom increased with the binding energy shifts, indicating fundamental differences compositional shifts between 700 °C and 1000 °C/1200 °C exposures. Based on the reported XPS binding energies,[31] the binding energy of Si 2*p* and Zr 3*d* at 1000 and 1200 °C corresponded to SiO_2 and ZrO_2 but those in 700 °C did not clearly match with the simple oxides. The shifts in x-ray photoelectron peaks are likely associated with a transition in binding states. Such shifts have been reported in a complex mixed oxide (i.e., $ZrSiO_4$) in comparison to simple oxides (i.e., ZrO_2 and SiO_2) due to different covalency of cations. The Si 2*p* bonding is more covalent but the Zr 3*d* is more ionic in $ZrSiO_4$.[32,33] Therefore, it is speculated that at 700 °C an amorphous Zr–Si–O phase forms, however, at

https://doi.org/10.1557/jmr.2016.363 Published online by Cambridge University Press



(d)

at.%	C-K	O-K	Si-K	Zr-L	Zr:Si
Pt. 1	-	21.26	70.79	7.94	1:8.9
Pt. 2	2.38	24.00	63.62	9.99	1:6.4
Pt. 3	2.70	52.56	26.05	18.70	1:1.4
Pt. 4	2.84	54.48	23.79	18.90	1:1.3

FIG. 5. Plan-view of SEM images of (a) as-received $ZrSi_2$, (b) $ZrSi_2$ oxidized at 700 °C for 5 h, (c) high voltage SEM (12 kV) image of the oxidized sample, and (d) EDS compositions in regions indicated in (c). Points 1 and 2 indicate the regions of spherical phases shown in the image (b).

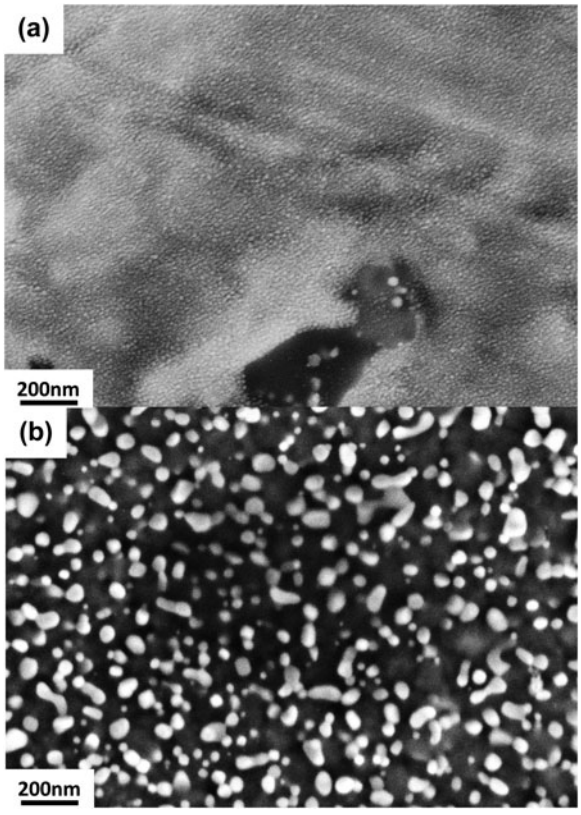


FIG. 6. Plan-view of high magnification SEM images of $ZrSi_2$ oxidized at (a) 1000 °C for 15 h and (b) 1200 °C for 5 h.

1000 and 1200 °C this phase is not stable but rather decomposes to distinct SiO_2 and ZrO_2 simple oxide phases. This is also in good agreement with phase conversion from amorphous $ZrSiO_4$ film to simple oxides at 900 °C annealing (i.e., Si–O–Zr → O–Si–O + O–Zr–O) reported in a previous study.[34,35] Interestingly, oxidation product of $TiSi_2$ at 600 °C in oxygen is glassy Ti–Si–O phase as well.[36] The near-surface chemical composition of oxidized surfaces as determined by the XPS technique is summarized in Table I. The variation of the concentration ratio of Zr to Si indicates that there was not only lateral diffusion of species shown in Figs. 5 and 6 but also depth-wise diffusion of species. The compositional ratio of Si to Zr was slightly reduced (less Si) at 700 °C but it increased again (more Si) at 1000 °C and gets doubled at 1200 °C compared to the as-received $ZrSi_2$. Based on the published high diffusion rate of Si compared to Zr,[37,38] it appears that a part of newly formed Si during oxidation diffused inward in the thin oxide layer so that the Si concentration on the surface is diminished during oxidation at 700 °C. However, a net outward flux of Si atoms at the higher temperatures increases the Si concentration on the outer-most surface.

2. Depth-wise structural evolution

To correlate the observed surface chemical and morphological evolution with depth-wise species diffusion, cross-sectional analysis using high magnification STEM imaging was performed (Fig. 8). At 700 °C, 10 h oxidation was carried out to get thicker oxide layer and subsequent STEM analysis showed dark wavy structures [Fig. 8(a)] in the ~630 nm thick oxide layer that formed. EDS line scan analysis showed the structures to be Si-rich oxide phase [Fig. 8(b)] and consequently a reduction of Si concentration was identified in the adjacent regions. Based on the STEM observation, the phase identification in XRD, and the binding energy shift in XPS, the major

https://doi.org/10.1557/jmr.2016.363 Published online by Cambridge University Press

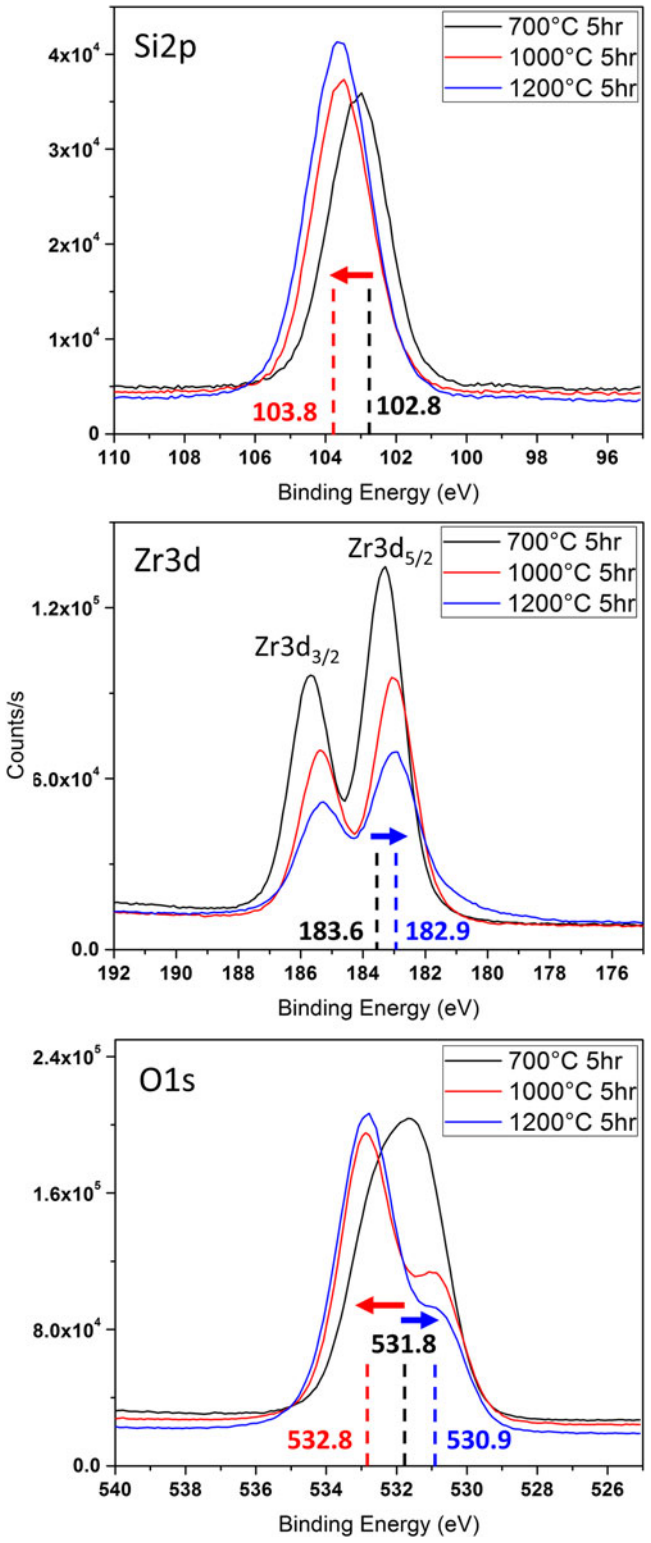


FIG. 7. XPS spectrum (Si 2*p*, Zr 3*d*, O 1*s* binding energy) of $ZrSi_2$ oxidized at 700, 1000, and 1200 °C after 5 h oxidation. Position of the peak maximum (eV) is specified and the arrows indicate the trend of binding energy shift with increasing temperature (from 700 °C to 1000 °C/1200 °C). The red arrows and blue arrows are associated with silicon and zirconium, respectively.

TABLE I. XPS near-surface chemical compositional analysis of as-received and $ZrSi_2$ oxidized at high temperatures.

Atomic%	Si 2*p*	Zr 3*d*	C 1*s*	O 1*s*	Zr:Si
As-polished	32.23	13.59	8.35	45.84	1.0:2.4
700 °C for 5 h	21.16	11.40	1.79	65.64	1.0:1.8
1000 °C for 5 h	23.38	8.60	3.37	64.65	1.0:2.7
1200 °C for 5 h	27.86	6.74	1.69	63.72	1.0:4.1

phases in the oxide layer at 700 °C are likely amorphous Zr–Si–O and Si-rich oxide. The cross-sectional images of samples oxidized at 1000 and 1200 °C showed complex nano/micron structures. Four types of structures were identified in the 7 μm oxide layer formed at 1000 °C [please see Figs. 8(c) and 8(d)]: (i) submicron layer with fine structural features, (ii) underlying wavy dark structures, (iii) a thick region consisting of irregular structures, and (iv) unreacted $ZrSi_2$ region. It is speculated that the wavy structures developed by the inward diffusion of Si at the early stages of oxidation and the nondirectional irregular structures were formed by spinodal decomposition in the amorphous Zr–Si–O matrix, which will be discussed in detail.

Similar evolution of the oxide structures was observed for samples oxidized at 1200 °C for 5 h. A large numbers of Si islands indicated by the red arrow in Fig. 9(a) were identified at the interface between the oxide layer and unreacted $ZrSi_2$. In addition, charging effects were observed in Fig. 9(a), indicating a fully oxidized structure (bright regions) which has dielectric properties. However, some regions appeared not to be oxidized significantly and manifested as dark and gray areas shown in Fig. 9(b). The nanoscale spherical particulates, which was seen on the plan view image [Fig. 6(b)], were dispersed only in region adjacent to air interface [Fig. 9(c)]. The uniform irregular nanoscale structures are again observed in Fig. 9(d). The EDS analysis [Fig. 10(a)] showed that the less oxidized regions were composed of Si-rich oxide and unreacted $ZrSi_2$. The origin of the Si-rich oxide is the slow reaction kinetics of SiO_2 growth[27] during oxidation of the newly formed Si and some $ZrSi_2$ were not completely consumed while the oxide layer was developing. The irregular structures seem to consist of ZrO_2 and SiO_2 based on the EDS point scan [point 1 in Fig. 10(b)], corresponding to the Si-depleted regions in the EDS mapping. In addition, the existence of Si islands in the interface between the oxide scale and $ZrSi_2$ suggests that the selective oxidation occurs at temperatures higher than those reported in temperature (<800 °C).[21] Due to relatively large SEM-EDS spot size (~1 μm), TEM-EDS analysis was performed to understand mechanism of evolution of this compositionally alternating oxide structure.

https://doi.org/10.1557/jmr.2016.363 Published online by Cambridge University Press

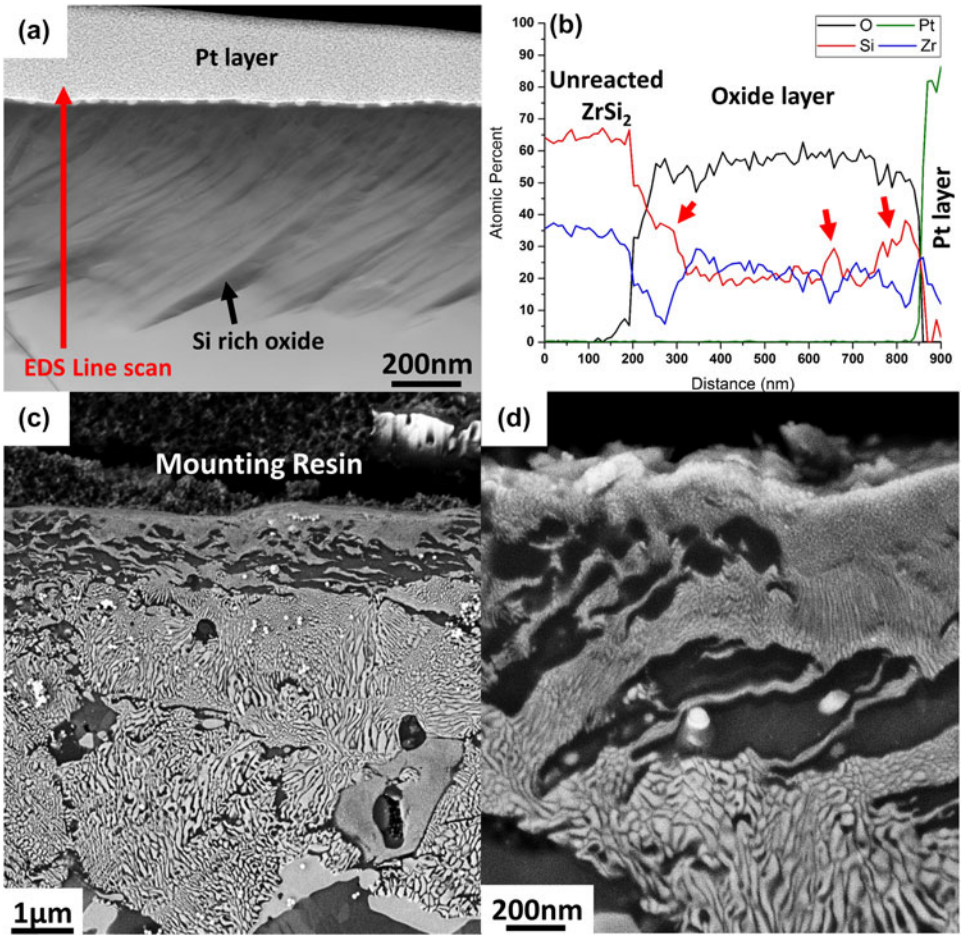


FIG. 8. (a) HAADF STEM cross-sectional image of $ZrSi_2$ oxidized at 700 °C for 10 h and (b) corresponding EDS line-scan showing composition fluctuation even in the thin (~630 nm) oxide layer. The red arrows indicate Si-rich oxide. (c) Cross-sectional SEM image with low voltage (3 kV) of the oxide layer on $ZrSi_2$ formed at 1000 °C for 5 h at low magnification and (d) and high magnification near the top layer.

The irregular nanoscale structures and spherical phases observed in Figs. 9(c) and 9(d) were analyzed using STEM-EDS (Fig. 11). The high angle annular dark field (HAADF) STEM images of the $ZrSi_2$ oxidized at 1200 °C for 5 h revealed nanoscale particulate phases [Fig. 11(a)] adjacent to the air interface and the irregular structures [Fig. 11(b)] uniformly dispersed in the entire oxide scale. Since brightness in HAADF images is proportional to atomic number of material, it is speculated that the structures were composed of higher atomic number elements compared to the background matrix material. STEM-EDS analysis confirmed the chemical composition of the structures as shown in Fig. 11(c). The spherical particulates and irregular structures were crystalline ZrO_2 in SiO_2 background matrix. The fuzzy ring diffraction pattern [inset, Fig. 11(b)] of the background matrix suggests that the SiO_2 phase is amorphous, in agreement with the XRD result where no crystalline SiO_2 peaks were identified.

IV. DISCUSSION

A. Spinodal decomposition

As mentioned earlier, a plausible explanation to the formation of an alternating nanolayered structure of ZrO_2 and SiO_2 is phase separation of amorphous Zr–Si–O by spinodal decomposition, a diffusion driven process that occurs in unstable undercooled or supersaturated phases, resulting in homogenous two-phase fine scale mixture.[39] Lucovsky et al.[34,35] first reported that annealing of ~400 nm amorphous $ZrSiO_4$ thin film at 900 °C for 60 s led to chemical phase separation consisting of crystalline ZrO_2 and amorphous SiO_2 based on infrared absorption spectroscopy. A thermodynamic driving force exists if the solid mixture is within unstable spinodal boundary. Kim et al.[40] estimated the excess Gibbs free energy of mixing in supercooled liquid of ZrO_2 and SiO_2 using a subregular model utilizing the invariant points in pseudo-binary ZrO_2–SiO_2 phase diagram. In addition, Stemmer et al.[41] predicted extension of the liquid

https://doi.org/10.1557/jmr.2016.363 Published online by Cambridge University Press

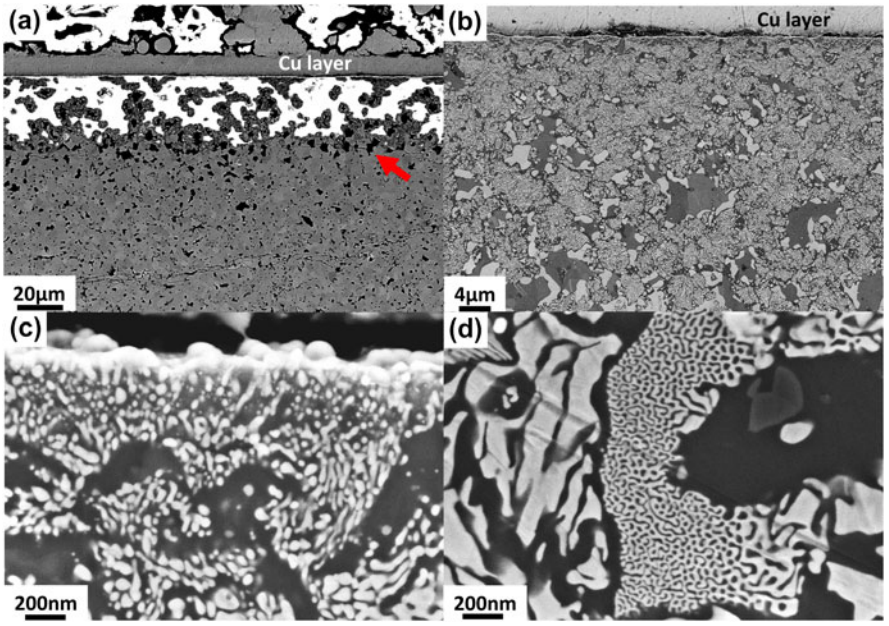
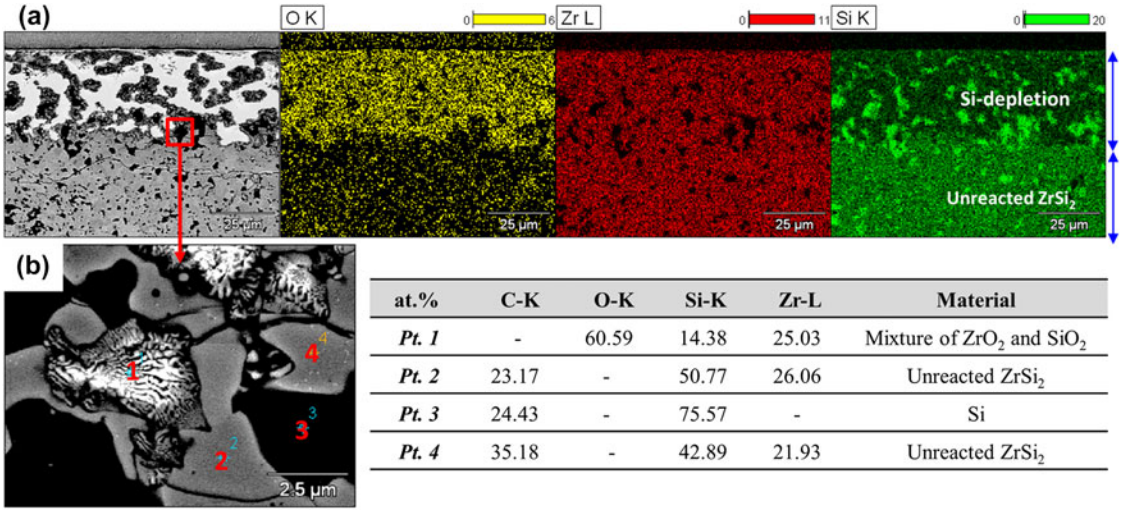


FIG. 9. SEM images of $ZrSi_2$ oxidized at 1200 °C for 5 h, taken at (a) 12 kV and (b) 3 kV at low magnifications. High magnification 3 kV SEM images (c) at interface between air and oxide layer and (d) at the middle of oxide scale showing different shapes of nanoscale structures.



at.%	C-K	O-K	Si-K	Zr-L	Material
Pt. 1	-	60.59	14.38	25.03	Mixture of ZrO_2 and SiO_2
Pt. 2	23.17	-	50.77	26.06	Unreacted $ZrSi_2$
Pt. 3	24.43	-	75.57	-	Si
Pt. 4	35.18	-	42.89	21.93	Unreacted $ZrSi_2$

FIG. 10. EDS spectra mapping (a) of the oxidized $ZrSi_2$ at 1200 °C for 5 h showing Si depleted region, and point EDS analysis (b) at the interface between oxide layer and unreacted $ZrSi_2$. The carbon signal is an artifact from the mounting resin.

miscibility gap and spinodals to lower temperature using commercially available thermodynamic software and published oxide data. Based on their estimations, the composition of spinodal boundary between 1000 and 1200 °C in ZrO_2 and SiO_2 mixture is in the range of 0.4–0.9 SiO_2 mole fraction and its corresponding decomposed equilibrium phases are ZrO_2 rich phase (0.2–0.4 SiO_2 mole fraction) and SiO_2 rich phase (0.9–0.98 SiO_2 mole fraction). Therefore, it is suggested that there is a thermodynamic driving force that induces spinodal decomposition in $ZrSi_2$ oxidation at high temperatures.

At 1000 °C, the spinodal structures near the top surface were finer than those at the center of the oxide layer, which may be attributed to ZrO_2/SiO_2 composition effect on Gibbs free energy of mixing. The minimum wave length of phase modulation decreases with increasing negativity of second derivative of Gibbs free energy of mixing.[42] The absolute value of the negative free energy is maximized at 73% mole fraction of SiO_2 at 1000 °C calculated by the subregular model,[41] which is consistent with Si concentration of the 1000 °C surface, resulting in formation of the finer spinodal structures.

https://doi.org/10.1557/jmr.2016.363 Published online by Cambridge University Press

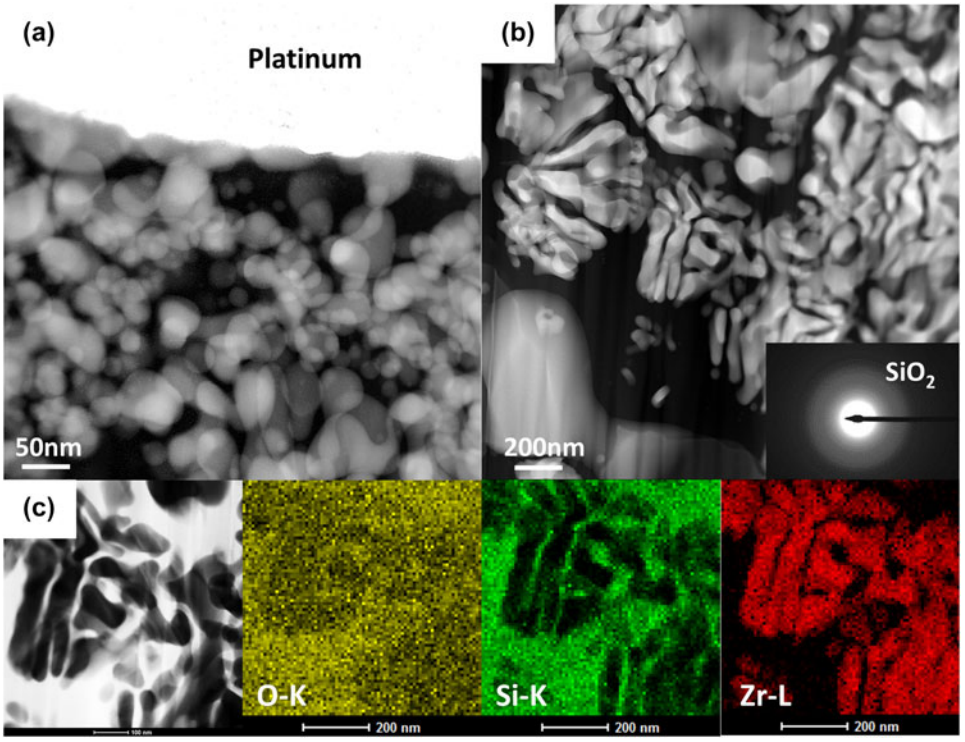


FIG. 11. HAADF STEM cross-sectional images of $ZrSi_2$ oxidized at 1200 °C for 5 h. (a) nanoscale spherical phases at the interface with air (i.e., top surface) and (b) irregular structures uniformly dispersed in oxide scale. The inset shows SiO_2 diffraction pattern indicating an amorphous structure. The platinum layer was deposited on the top of the sample during sample preparation by FIB. Higher atomic number material has brighter contrast in these images. (c) Bright field STEM image and STEM-EDS elemental mapping images of the irregular structures. These images clearly indicate that the irregular structures consist of ZrO_2 and amorphous SiO_2.

Additionally, nucleation of the ZrO_2 particulates at 1200 °C on the top surface would also be explained by the extension of the liquid miscibility gap. Due to the highest concentration of SiO_2 on the top surface by outward Si diffusion in oxide layer (see Table I) at 1200 °C, the composition may not be within the spinodal boundary but within miscibility gap. Therefore, nucleation and growth of ZrO_2 in SiO_2 matrix will likely lower its free energy in lieu of spinodal decomposition.

B. Kinetic suppression of crystalline $ZrSiO_4$ formation

It is worth noting that crystalline $ZrSiO_4$ was not identified in the $ZrSi_2$ oxidation even though its formation is preferable in binary ZrO_2–SiO_2 phase diagram at the temperatures with any composition.[43] Most published experiments agree that $ZrSiO_4$ formation from a reaction of ZrO_2 and SiO_2 requires at least 1300 °C annealing temperature.[44–47] Formation of crystalline $ZrSiO_4$ is a solid state reaction, hypothesized that Si^{4+} cations from amorphous SiO_2 diffuses through the highly refractory $ZrSiO_4$ layer and reacts with t-ZrO_2 to produce new phase and there are no mobile species like in liquid or gas.[45] Therefore, the growth rate of crystalline $ZrSiO_4$ is kinetically limited although thermodynamically favored. Crystalline $ZrSiO_4$ formation is expected in $ZrSi_2$ oxidation at higher temperature (e.g., 1300 °C or 1400 °C) or much longer time oxidation.

C. Summary of $ZrSi_2$ oxidation

Based on the analysis in this study, a physical model for microstructural evolution during the isothermal oxidation at each test temperature is schematically shown in Fig. 12 in an attempt to develop a picture of microstructural evolution in the oxide layer. At 700 °C, a thin oxide layer consisting of Zr–Si–O amorphous phase matrix with Si-rich oxide wavy structures forms. Additionally, small amount of Si and ZrO_2 was identified in XRD analysis. The role of the newly formed Si by the selective oxidation in the $ZrSi_2$ oxidation is important. The Si diffuses around the oxide layer and leads to the formation of Si-rich spherical phases on the surface and its inward diffusion induced reduction of Si concentration on the top surface as well as formed Si-rich wavy oxide. Although the composition of the oxide is within the estimated spinodal boundary, mobility of species at this temperature is not enough to show distinct phase separation.

At 1000 °C, in the initial stages of oxidation, the Si diffused inward first when it reacted with oxygen in the thin oxide layer and agglomerated resulting in

https://doi.org/10.1557/jmr.2016.363 Published online by Cambridge University Press

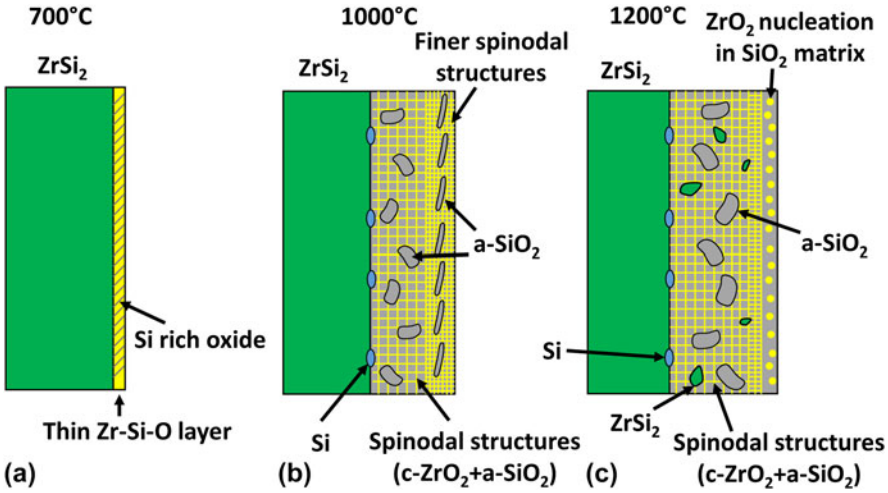


FIG. 12. Schematic illustration of the microstructural evolution during isothermal oxidation of $ZrSi_2$ oxidation at (a) 700 °C, (b) 1000 °C, and (c) 1200 °C. c = crystalline and a = amorphous. The figure is not scaled.

wavy Si-rich oxide structures. The wavy structures seen in 700 °C oxidation tests were likely precursors of those observed at 1000 °C. While oxidation continues, outward diffusion of the newly formed Si dominated as confirmed by the increment of Si concentration at the surface. In the oxide/$ZrSi_2$ interface, the amorphous Zr–Si–O mixture decomposed quickly so that the isotropic irregular structures consisting of ZrO_2 and SiO_2 were generated. At the same time, the Si produced Si-rich oxide islands near the spinodal structures.

At 1200 °C, the oxidation behavior was similar to 1000 °C oxidation except for the nucleation of the nanoscale ZrO_2 particulates near the air interface. Due to remarkable outward diffusion of Si ions, the Zr–Si–O mixture was metastable and reduced its free energy by ZrO_2 nucleation. In short, it is suggested that an intermediate unstable Zr–Si–O mixture exists during oxidation of $ZrSi_2$ at 1000 and 1200 °C, leading to phase separation to ZrO_2 and SiO_2.

V. CONCLUSIONS

A study to gain and fundamental understanding of the evolution of oxide layer in $ZrSi_2$ at high temperatures has been performed with the goal of applying $ZrSi_2$ coatings on Zr-alloy fuel cladding to improve their accident tolerance. $ZrSi_2$ showed parabolic-cubic oxidation kinetics depending on temperature and its weight gain due to oxidation was negligible compared to Zr-4. Average oxide scale thickness was 470 nm, 6.7 μm, and 37 μm at 700 °C, 1000 °C, and 1200 °C, respectively, for 5 h oxidation. The oxide scale was mechanically stable and there was no evidence of spallation of the oxide layer. At 700 °C, the surface morphology changed in that Si-rich micron-sized spherical phases on the top surface and Si-rich wavy structures in amorphous Zr–Si–O layer were observed. At 1000 °C, the Si concentration increased at the surface. In the depth-wise direction, fine spinodal structures, wavy Si-rich oxide, coarse spinodal structures, and Si-rich oxide islands were developed. At 1200 °C, similar structures were observed and additionally ZrO_2 particulates in air interface. SEM-EDS and STEM-EDS analysis confirmed spinodal decomposition of Zr–Si–O matrix at 1000 and 1200 °C resulting crystalline ZrO_2 and amorphous SiO_2 and the driving force of their formation was explained by phase instability at 1000 and 1200 °C in ZrO_2–SiO_2 pseudo-binary phase diagram. Formation of finer spinodal structures at 1000 °C and nucleation of spherical ZrO_2 particulates at 1200 °C may be attributed to high SiO_2 mole fraction by outward Si diffusion. A physical model for oxidation has been proposed wherein Zr–Si–O mixture with newly formed Si undergoes a spinodal phase decomposition into ZrO_2 and SiO_2, which manifested as a nanoscale assembly of alternating layer of the two oxides. Based on its high oxidation resistance, $ZrSi_2$ can be considered as a potential candidate coating material for LWR Zr-alloy fuel cladding for improved accident tolerance during a loss of coolant accident. The high temperature oxidation resistance results from the formation of amorphous Zr–Si–O or glassy SiO_2. However, more tests particularly in steam environment and coating fabrication approaches must be investigated for implementation of this application.

ACKNOWLEDGMENTS

The authors are grateful to Steven Fronek for sample preparation and Alexander Mairov for technical support with STEM. This work is funded by Department of Energy (DOE) through grants DE-NE0008300.

https://doi.org/10.1557/jmr.2016.363 Published online by Cambridge University Press

REFERENCES

1. G. Sabol, R.J. Comstock, R. Weiner, P. Larouere, and R. Stanutz: In-reactor corrosion performance of ZIRLO and Zircaloy-4. In *Zirconium in the Nuclear Industry: Tenth International Symposium* (American Society for Testing and Materials, Philadelphia, 1994); p. 724.
2. B.A. Pint, K.A. Terrani, M.P. Brady, T. Cheng, and J.R. Keiser: High temperature oxidation of fuel cladding candidate materials in steam–hydrogen environments. *J. Nucl. Mater.* **440**, 420 (2013).
3. M. Steinbrück: Prototypical experiments relating to air oxidation of Zircaloy-4 at high temperatures. *J. Nucl. Mater.* **392**, 531 (2009).
4. M. Steinbrück and M. Böttcher: Air oxidation of Zircaloy-4, M5® and ZIRLO™ cladding alloys at high temperatures. *J. Nucl. Mater.* **414**, 276 (2011).
5. J.H. Baek and Y.H. Jeong: Breakaway phenomenon of Zr-based alloys during a high-temperature oxidation. *J. Nucl. Mater.* **372**, 152 (2008).
6. T. Cheng, J.R. Keiser, M.P. Brady, K.A. Terrani, and B.A. Pint: Oxidation of fuel cladding candidate materials in steam environments at high temperature and pressure. *J. Nucl. Mater.* **427**, 396 (2012).
7. M. Ben-Belgacem, V. Richet, K.A. Terrani, Y. Katoh, and L.L. Snead: Thermo-mechanical analysis of LWR SiC/SiC composite cladding. *J. Nucl. Mater.* **447**, 125 (2014).
8. K.A. Terrani, S.J. Zinkle, and L.L. Snead: Advanced oxidation-resistant iron-based alloys for LWR fuel cladding. *J. Nucl. Mater.* **448**, 420 (2014).
9. Y. Yamamoto, B. Pint, K.A. Terrani, K. Field, S. Maloy, and J. Gan: Progress towards the development of nuclear grade FeCrAl fuel cladding. In *TopFuel 2015*, Vol. **467** (European Nuclear Society, Zurich, 2015); p. 703.
10. I. Idarraga-trujillo, M. Le flem, J-C. Brachet, M. Le Saux, D. Hamon, and S. Muller: Assessment at CEA of coated nuclear fuel cladding for LWRs with increased margins in LOCA and beyond LOCA conditions. In *Proc. TopFuel 2013* (American Nuclear Society, Charlotte, 2013); p. 860.
11. H-G. Kim, I-H. Kim, Y-I. Jung, D-J. Park, J-Y. Park, and Y-H. Koo: Adhesion property and high-temperature oxidation behavior of Cr-coated Zircaloy-4 cladding tube prepared by 3D laser coating. *J. Nucl. Mater.* **465**, 531 (2015).
12. B.R. Maier, B.L. Garcia-Diaz, B. Hauch, L.C. Olson, R.L. Sindelar, and K. Sridharan: Cold spray deposition of Ti_2AlC coatings for improved nuclear fuel cladding. *J. Nucl. Mater.* **466**, 712 (2015).
13. J.H. Sung, T.H. Kim, and S.S. Kim: Fretting damage of TiN coated Zircaloy-4 tube. *Wear* **250**, 658 (2001).
14. R. Mitra: Mechanical behaviour and oxidation resistance of structural silicides. *Int. Mater. Rev.* **51**, 13 (2006).
15. A.A. Sharif: High-temperature oxidation of $MoSi_2$. *J. Mater. Sci.* **45**, 865 (2010).
16. S. Knittel, S. Mathieu, and M. Vilasi: The oxidation behaviour of uniaxial hot pressed $MoSi_2$ in air from 400 to 1400 °C. *Intermetallics* **19**, 1207 (2011).
17. R. Rosenkranz and G. Frommeyer: Microstructures and properties of the refractory compounds $TiSi_2$ and $ZrSi_2$. *Z. Metallkd.* **83**, 685 (1992).
18. W.J. Strydom, J.C. Lombaard, and R. Pretorius: Thermal oxidation of the silicides $CoSi_2$, $CrSi_2$, $NiSi_2$, $PtSi_2$, $TiSi_2$ and $ZrSi_2$. *Thin Solid Films* **131**, 215 (1985).
19. P. Pérez, M. López, J. Jiménez, and P. Adeva: Oxidation behaviour of Al-alloyed $ZrSi_2$ at 700 °C. *Intermetallics* **8**, 1393 (2000).
20. P. Pérez: Oxidation behavior of Al-alloyed $ZrSi_2$. *Oxid. Met.* **56**, 163–176 (2001).
21. H. Geßwein, A. Pfrengle, J.R. Binder, and J. Haußelt: Kinetic model of the oxidation of $ZrSi_2$ powders. *J. Therm. Anal. Calorim.* **91**, 517 (2007).
22. D. Gosset and M. Le Saux: In-situ x-ray diffraction analysis of zirconia layer formed on zirconium alloys oxidized at high temperature. *J. Nucl. Mater.* **458**, 245 (2014).
23. S.P. Murarka: *Silicides for VLSI Applications*, 1st ed. (Academic Press, Cambridge, 2012).
24. S. Becker, A. Rahmel, and M. Schutze: Oxidation of $TiSi_2$ and $MoSi_2$. *Solid State Ionics* **53–56**, 280 (1992).
25. Y. Liu, G. Shao, and P. Tsakiropoulos: On the oxidation behaviour of $MoSi_2$. *Intermetallics* **9**, 125 (2001).
26. A.S. Khanna: *Introduction to high temperature oxidation and corrosion*. 1st ed. (ASM International, Materials Park, 2002).
27. D. Lafatzis and K. Mergia: Oxidation behaviour of Si wafer substrates in air. *J. Appl. Phys.* **114**, 1 (2013).
28. L.N. Lie, W.A. Tiller, and K.C. Saraswat: Thermal oxidation of silicides. *J. Appl. Phys.* **56**, 2127 (1984).
29. D.A. Berztiss, R.R. Cerchiara, E.A. Gulbransen, F.S. Pettit, and G.H. Meier: Oxidation of $MoSi_2$ and comparison with other silicide materials. *Mater. Sci. Eng., A* **155**, 165 (1992).
30. V.F. Urbanic and T.R. Heidrick: High-temperature oxidation of Zircaloy-2 and Zircaloy-4 in steam. *J. Nucl. Mater.* **75**, 251 (1978).
31. A. Naumkin, A. Kraut-Vass, S. Gaarenstroom, and C. Powell: Nist x-ray photoelectron spectroscopy database. (2012). Available at: http://srdata.nist.gov/xps/Default.aspx.
32. M.J. Guittet, J.P. Crocombette, and M. Gautier-Soyer: Bonding and XPS chemical shifts in $ZrSiO_4$ versus SiO_2 and ZrO_2: Charge transfer and electrostatic effects. *Phys. Rev. B: Condens. Matter Mater. Phys.* **63**, 125117 (2001).
33. A.P. Dementjev: Altered layer as sensitive initial chemical state indicator*. *J. Vac. Sci. Technol., A* **12**, 423 (1994).
34. G. Rayner, R. Therrien, and G. Lucovsky: The structure of plasma-deposited and annealed pseudo-binary ZrO_2–SiO_2 alloys. *Mater. Res. Soc. Symp. Proc.* **611**, C1.3.1 (2000).
35. G. Lucovsky and G.B. Rayner: Microscopic model for enhanced dielectric constants in low concentration SiO_2-rich noncrystalline Zr and Hf silicate alloys. *Appl. Phys. Lett.* **77**, 2912 (2000).
36. F. Schwettmann, R. Graff, and M. Kolodney: Mechanism of the oxidation of titanium disilicide. *J. Electrochem. Soc.* **118**, 1973 (1971).
37. D.J. Tallman, J. Yang, L. Pan, B. Anasori, and M.W. Barsoum: Reactivity of Zircaloy-4 with Ti_3SiC_2 and Ti_2AlC in the 1100–1300 °C temperature range. *J. Nucl. Mater.* **460**, 122 (2015).
38. S. Roy and A. Paul: Growth of hafnium and zirconium silicides by reactive diffusion. *Mater. Chem. Phys.* **143**, 1309 (2014).
39. D.E. Laughlin and W. Soffa: Spinodal structures. In *ASM Handbook*, Vol. **9** (ASM International, Materials Park, 1985); p. 652.
40. H. Kim and P.C. McIntyre: Spinodal decomposition in amorphous metal-silicate thin films: Phase diagram analysis and interface effects on kinetics. *J. Appl. Phys.* **92**, 5094 (2002).
41. S. Stemmer, Z. Chen, C. Levi, P. Lysaght, B. Foran, and J. Gisby: Application of metastable phase diagrams to silicate thin films for alternative gate dielectrics. *Jpn. J. Appl. Phys., Part 1* **42**, 3593 (2003).
42. D. Porter and K. Easterling: *Phase Transformations in Metals and Alloys*, 1st ed. (Van Nostrand Reinhold, New York, 1981).
43. W.C. Butterman and W.R. Foster: Zircon stability and the ZrO_2–SiO_2 phase diagram. *Am. Mineral.* **52**, 880 (1967).
44. T. Itoh: Formation of polycrystalline zircon ($ZrSiO_4$) from amorphous silica and amorphous zirconia. *J. Cryst. Growth* **125**, 223 (1992).
45. C. Veytizou, J.F. Quinson, O. Valfort, and G. Thomas: Zircon formation from amorphous silica and tetragonal zirconia: Kinetic study and modelling. *Solid State Ionics* **139**, 315 (2001).
46. S. Ramani, E. Subbarao, and K. Gowhale: Kinetics of zircon synthesis. *J. Am. Ceram. Soc.* **52**, 619 (1969).
47. A. Kaiser, M. Lobert, and R. Telle: Thermal stability of zircon ($ZrSiO_4$). *J. Eur. Ceram. Soc.* **28**, 2199 (2008).

https://doi.org/10.1557/jmr.2016.363 Published online by Cambridge University Press